

Learning-Performance Evaluation of a Physical Reservoir Based on a Vortex Spin-Torque Oscillator with a Modified Free Layer

Kota Horizumi,¹ Takahiro Chiba,^{2,3} and Takashi Komine¹

¹*Graduate School of Science and Engineering, Ibaraki University, Hitachi, Ibaraki 316-8511, Japan*

²*Department of Information Science and Technology, Graduate School of Science and Engineering, Yamagata University, Yonezawa, Yamagata 992-8510, Japan*

³*Department of Applied Physics, Graduate School of Engineering, Tohoku University, Sendai, Miyagi 980-8579, Japan*

(Dated: 3 March 2026)

In this study, we numerically evaluate the learning performance of a vortex spin-torque oscillator with a modified free layer, called a modified VSTO (m-VSTO), in which an additional layer (AL) of smaller radius is stacked on the free layer, for physical reservoir computing. The vortex-core dynamics are computed using the Thiele equation incorporating the potential deformation induced by the AL. We identify the edge of chaos from the maximal Lyapunov exponent and quantify the short-term memory capacity (STMC) as well as the information processing capacity (IPC) in a time-multiplexed reservoir scheme. We find that the m-VSTO exhibits finite STMC and IPC in a low-current and low-field regime below the threshold current of the conventional VSTO, and can achieve up to approximately twice the IPC with about one quarter of the power consumption. Furthermore, when the input pulse width is set comparable to or longer than the transient time, the parameter region with high STMC and IPC expands, and the optimal operating region is located not at the edge of chaos but in a stable regime with long transients. These results suggest that engineering the potential landscape and the driving conditions enables low-power spintronic physical reservoirs.

Physical reservoir computing (PRC), which exploits nonlinear dynamics in physical systems for information processing, has attracted considerable attention as an energy-efficient hardware platform for machine learning.^{37,38} As a widely discussed guideline, PRC performance is often reported to be high near the so-called edge of chaos (EoC), *i.e.*, close to the transition between ordered and chaotic dynamics.^{39,40} To date, a variety of physical systems have been proposed as PRC candidates, including optical systems⁴¹ and mechanical systems.⁴² Among them, spintronic devices are promising because they enable compact and high-speed information processing, and have therefore been actively investigated.^{43–47} A representative example is the vortex spin-torque oscillator (VSTO), which has been studied with PRC applications in mind.^{48–53}

However, because the conventional VSTO requires a finite threshold current to sustain self-oscillation, it is difficult to sufficiently reduce the operating current, which limits its energy efficiency.^{54–56} Moreover, it has been pointed out that, in VSTOs, the short-term memory capacity (STMC), which quantifies how much past input a reservoir can retain,⁵⁷ and the information processing capacity (IPC), which evaluates how accurately the reservoir can realize complex nonlinear mappings,⁵⁸ are not necessarily maximized at the EoC; thus, the relationship between nonlinearity and learning performance remains unclear.^{59,60}

In this Letter, we systematically evaluate, through numerical simulations, the learning performance of the modified VSTO (m-VSTO) that we recently proposed.^{61,62} In an m-VSTO, the potential landscape is modified by the presence of a small-radius AL on the free layer, which endows the device with strong nonlinearity that can produce chaotic dynamics under an applied ac magnetic field, while also enabling self-oscillation at lower currents than in a conventional VSTO. (i) We first compute the dependence of the maximal Lyapunov exponent,⁶⁵ a standard indicator of chaos, on the dc current and external magnetic field to identify the EoC region exhibited by the m-VSTO. (ii) We then evaluate the STMC and IPC in the same parameter space and examine in detail the relationship between the Lyapunov exponent and these learning-performance metrics. (iii) To explain why high STMC/IPC can emerge away from the EoC, we show that the learning performance is governed by the transient time associated with the m-VSTO’s below-threshold oscillations and its timescale matching with the input pulse width. Based on this relation, we propose pulse-width settings that maximize STMC/IPC under low-current operation, thereby identifying conditions for simultaneously achieving low-power operation and enhanced learning performance.

As shown in Fig. 1(a), we consider an m-VSTO in which a circular ferromagnetic AL made of the same material as the free layer, but with a smaller radius than the free layer, is concentrically stacked on the free layer with the radius R and the thickness L of a VSTO composed of a ferromagnet/insulator/ferromagnet trilayer. We employ a Cartesian coordinate system whose origin is at the center of the free layer and denote the basis vectors by \mathbf{e}_k ($k = x, y, z$). In the presence of a dc-current-induced spin torque and an external magnetic field \mathbf{H} , the motion of the vortex-core position \mathbf{X} is described by the Thiele equation:^{60–62,66–69}

$$\begin{aligned}
& -G\mathbf{e}_z \times \dot{\mathbf{X}} - |D|(1 + \xi s^2)\dot{\mathbf{X}} - \frac{\partial W(s)}{\partial \mathbf{X}} \\
& + a_J J m_z \mathbf{e}_z \times \mathbf{X} + ca_J R_0 m_x \mathbf{e}_x + c\mu^* \mathbf{e}_z \times \mathbf{H} = \mathbf{0},
\end{aligned} \tag{1}$$

where $\mathbf{X} = (X, Y, 0)$ is the vortex core position vector, $\dot{\mathbf{X}}$ is the velocity vector, and $s = \sqrt{X^2 + Y^2}$ is the distance of the vortex core from the center of the free layer. Here, $W(s)$ is the potential function and $J = I/(\pi R^2)$ is the current density. The coefficient $a_J = \pi \hbar \sigma / (2e)$ characterizes the spin-transfer torque, and the other coefficients are given by $G = \frac{2\pi p M L}{\gamma}$, $D = -\frac{2\pi \alpha M L}{\gamma} (1 - \frac{1}{2} \ln \frac{R_0}{R})$, and $\mu^* = \pi M L R$. Here, M is the saturation magnetization, γ is the gyromagnetic ratio, α is the Gilbert damping constant, R_0 is the vortex-core radius, ξ is the nonlinear damping coefficient, σ is the spin polarization, $\mathbf{m} = (m_x, m_y, m_z)$ is the magnetization direction of the reference layer, p is the polarity, and c is the chirality. The external magnetic field is taken as $\mathbf{H} = (h_x, 0, 0)$. The VSTO consists of FeB/MgO/CoFeB multilayers. Unless otherwise stated, the parameters in Eq. (1) are set to $M = 1300 \text{ emu/cm}^3$, $\gamma = 1.764 \times 10^7 \text{ rad}/(\text{Oes})$, $\alpha = 0.01$, $\xi = 2$, and the spin polarization $P = 0.7$. We set the vortex polarity and chirality to $p = 1$ and $c = 1$, and use the vortex-core radius $R_0 = 10 \text{ nm}$. The free-layer radius and thickness are $R = 187.5 \text{ nm}$ and $L = 5 \text{ nm}$. For the m-VSTO, an additional FeB layer is concentrically stacked on the free layer with radius $R_a = 40 \text{ nm}$ and thickness $L_a = L/3$. The reference-layer magnetization direction is taken as $\mathbf{m} = (m_x, 0, m_z) = (\sin(\pi/3), 0, \cos(\pi/3))$. These parameter values follow the established VSTO/m-VSTO modeling in the literature.^{60–62}

For a conventional VSTO,⁶⁰ the potential can be approximated by a single-well form with a minimum at the center, $W(s) \simeq \frac{\kappa}{2}s^2 + \frac{\kappa'}{4}s^4$. In contrast, the potential of the m-VSTO takes a Mexican-hat-like (wine-bottle-like) form, featuring an annular minimum near the edge of the additional layer. The modified potential profile $W(s)$ for the vortex core

was obtained from micromagnetic simulations⁷⁰ using the two-vortices ansatz,⁷¹ assuming that the magnetizations in the free layer and the AL are strongly coupled via exchange interaction. The effect of the modified potential was incorporated into the Thiele equation through the restoring force term $-\partial W(s)/\partial \mathbf{X}$.

We have systematically investigated how the AL deforms the confinement potential and thereby endows the m-VSTO with novel functionalities.^{61,62} In conventional VSTOs, inducing chaotic dynamics typically requires engineered driving schemes, such as nanocontact geometries,^{63,64} delayed feedback,⁵⁶ or random magnetic fields.⁶⁰ By contrast, in the m-VSTO the AL reshapes the vortex-core confinement potential, effectively enhancing the nonlinearity of the restoring force and enabling chaotic vortex-core motion even without a dc current. As a representative example, we apply an x -directed sinusoidal field $h_x(t) = h_0 \sin(2\pi ft)$ with $f = 100$ MHz and $h_0 = 25$ Oe at $I = 0$, for which the trajectory becomes aperiodic and the gyration amplitude exhibits irregular fluctuations, indicating a chaotic response [Fig. 1(b),(c)]. Furthermore, when the initial vortex-core position is chosen near the annular groove (potential minimum) at $s \simeq s_0$, sustained gyration emerges even below the threshold current of the conventional VSTO, I_{th} ($I < I_{\text{th}}$), and the below-threshold oscillation frequency $f_{\text{below}}(I)$ depends approximately linearly on the applied current I . Unless otherwise stated, all m-VSTO simulations presented below are initialized with the vortex core placed near the annular minimum, *i.e.*, $s(0) \simeq s_0$, so that the dynamics starts from the groove-trapped state. As $I \rightarrow I_{\text{th}}$, $f_{\text{below}}(I)$ continuously connects to the conventional oscillation frequency f_{osci} , and for $I > I_{\text{th}}$ the oscillation frequencies of the conventional VSTO and the m-VSTO coincide. In practice, we prepare the groove-trapped initial state by a short preconditioning step: a dc-current drive is first applied to excite vortex gyration, and the core subsequently relaxes into the annular minimum, providing a reproducible initial condition.⁶² These characteristics—self-sustained dynamics in the low-current regime and a strong nonlinear response absent in conventional VSTOs—are well suited to PRC, where nonlinearity and transient responses serve as computational resources; accordingly, in this study we quantitatively evaluate how these properties influence learning-performance metrics such as STMC and IPC.

The Thiele equation was numerically solved to obtain the vortex-core dynamics, and the maximal Lyapunov exponent was computed using the Shimada–Nagashima method⁷² to identify the EoC. Furthermore, to evaluate the learning performance, we used a fixed-

pulse-width external magnetic field as the input, the normalized radius distance s as the output, and adopted a time-division multiplexing scheme. The output within each pulse interval was divided into 50 segments, simulating 50 virtual nodes. For the evaluations of STMC and IPC, the input sequences for training and testing were generated independently; after training the readout, we re-run the device dynamics from the same prescribed initial condition to construct the test reservoir states, so that no explicit washout is required in our protocol. The readout weights were obtained by ordinary least squares using the Moore-Penrose pseudoinverse. Unless otherwise stated, the re-initialization places the vortex core near the annular groove, $s(0) \simeq s_0$, to start from the groove-trapped state.

(i) We first compute the dependence of the maximal Lyapunov exponent on the dc current and external magnetic field to identify the EoC region exhibited by the m-VSTO. Figure 2 shows the dependence of the Lyapunov exponent λ on the external magnetic field amplitude and the applied dc current for a conventional VSTO and an m-VSTO. In these calculations, the x component of the external magnetic field \mathbf{H} is given by $h_x(t) = h_0 r(t)$, where $r(t)$ is a random pulse train with a fixed pulse width of 3 ns generated from a uniform distribution over $[-1, 1]$. The horizontal axis denotes the field amplitude h_0 ranging from 0 to 16 Oe, and the vertical axis denotes the applied current I ranging from 0 to 4 mA. A positive λ indicates chaotic dynamics, whereas a negative λ indicates nonchaotic (periodic) dynamics. We color-code the regions with $\lambda > 0$ in red and those with $\lambda < 0$ in blue, and we mark regions where λ is very close to zero ($|\lambda| \approx 0$) in white, which we regard as corresponding to the EoC.

For the conventional VSTO as shown in Fig. 2(a), as reported previously, self-oscillation emerges above the threshold current $I_{\text{th}} \simeq 2.1$ mA, and chaos is induced mainly at large field amplitudes. In contrast, for the m-VSTO as shown in Fig. 2(b)], the EoC already appears at currents below the threshold of the conventional device, and chaos is induced at lower field amplitudes than in the conventional VSTO. As a result, the m-VSTO exhibits a broad EoC region in the low-current and low-field regime.

(ii) Next, we evaluate the STMC and IPC in the same parameters and examine in detail the relationship between the Lyapunov exponent and these learning-performance metrics. Figure 3 shows the dependence of the learning-performance metrics, STMC and IPC, on the external-field strength and the dc current. In all calculations, the pulse width was fixed at 3 ns, whereas the input sequences used for the STMC and IPC evaluations were different.

For the STMC calculation, we set the sequence length to $N = 1000$, where N is the number of input signals, and defined the external field as $\mathbf{H}(t) = (h_0 r_b(t), 0, 0)$, where $r_b(t)$ is a binary random function that takes values 0 or 1. For the IPC calculation, we increased the sequence length to $N = 5000$ so that the estimated IPC value sufficiently converges, and we defined $\mathbf{H}(t) = (h_0 r(t), 0, 0)$ using a random function $r(t)$ drawn from a uniform distribution on $[-1, 1]$ to preserve orthogonality among nonlinear functions. Comparing Figs. 3(a) and 3(b), which show the results for the STMC C_{STM} , we find that the capacity is almost zero below the threshold current for the conventional VSTO, whereas the m-VSTO exhibits a finite value under the same conditions. Above the threshold current, the influence of the AL becomes small, and the results for the two devices nearly coincide. Similar trends are observed for the information processing capacity in Figs. 3(c) and 3(d). In particular, the IPC of the m-VSTO is maximized around $h_0 \simeq 1$ Oe and $I \simeq 1$ mA, reaching approximately twice the value of the conventional VSTO while consuming about one quarter of the power. Here the power consumption is estimated from Joule heating, $P \simeq I^2 R$, neglecting the bias dependence of the device resistance and assuming a comparable effective resistances of the conventional VSTO and the m-VSTO. Therefore, operating the m-VSTO at $I \simeq 1$ mA, which is about half of the threshold current of the conventional VSTO ($I_{\text{th}} \simeq 2$ mA), corresponds to approximately one quarter of the power consumption.

A comparison between Fig. 2 and Figs. 3(a) and 3(b) indicates that C_{STM} decreases as the system approaches the EoC and becomes almost zero in the chaotic regime. By contrast, C_{STM} tends to increase in regions where λ is negative with a large magnitude. The same tendency is also observed for the IPC, suggesting that the learning performance is enhanced not near the EoC but rather in the regime where the Lyapunov exponent takes the most negative values. This trend suggests that, in our pulsed-drive and time-multiplexed setting, the performance is governed not by proximity to the EoC per se but by how the pulse width matches the transient time of the below-threshold dynamics, which we discuss next.

(iii) To clarify why high STMC/IPC appears in a regime away from the EoC, we discuss how the interplay between the transient time below threshold and the input pulse width determines the sign and magnitude of the Lyapunov exponent, and we provide a guideline for choosing pulse widths that enhance learning performance under low-current operation. In our time-multiplexed scheme, a sufficiently negative λ suppresses divergence of nearby trajectories under pulsed perturbations, while a long transient enables the reservoir state to

retain information over multiple input steps; thus, the key resource is the transient timescale and its matching to the pulse width. Because the Lyapunov exponent quantifies whether the separation between two nearby trajectories increases or decreases exponentially, it directly reflects how rapidly perturbations are damped and therefore characterizes the transient relaxation of the dynamics. Figure 4 shows the Lyapunov exponent λ of the m-VSTO for pulse widths $t_p = 5, 7, 8,$ and 10 ns, demonstrating that, as t_p increases, the region with $\lambda < 0$ expands in the below-threshold regime and the EoC shifts toward higher field strengths. To connect this trend to a characteristic relaxation time, we linearize the Thiele equation near the annular groove formed by the additional layer and estimate the transient time in the below-threshold regime, *i.e.*, $I < I_{\text{th}}$. Using the polar representation $X + iY = se^{i\psi}$, we approximate the potential near the groove position s_0 as $W(s) \simeq (\kappa_0/2)(s-s_0)^2$ and treat the damping locally as a constant, $D'(s) = |D|(1+\xi s^2) \simeq D'(s_0)$, while defining $A_J(I) = a_{JP_z}J$. Under these approximations, Eq. (1) can be rewritten as

$$\begin{cases} Gs\dot{\psi} - D'(s)\dot{s} - \kappa_0(s-s_0) = 0, \\ -G\dot{s} - D'(s)s\dot{\psi} + A_J(I)s = 0. \end{cases} \quad (2)$$

Solving these equations for \dot{s} yields

$$\dot{s} = \frac{1}{G^2 + D'(s)^2} \{ (A_J(I)G - D'(s)\kappa_0)s + D'(s)\kappa_0s_0 \}, \quad (3)$$

from which the steady-state radius s^* satisfying $\dot{s} = 0$ is obtained as

$$s^* = \frac{-D'(s)\kappa_0s_0}{A_J(I)G - D'(s)\kappa_0}. \quad (4)$$

Linearizing around the steady orbit $s = s^*$ by setting $s = s^* + \delta s$, we obtain

$$\dot{\delta s} = \frac{1}{G^2 + D'(s)^2} (A_J(I)G - D'(s)\kappa_0)\delta s. \quad (5)$$

The perturbation therefore decays as $\delta s(t) = \delta s(0)e^{-\gamma t}$, and the transient time is given by $\tau_{\text{below}} = 1/\gamma$, *i.e.*,

$$\tau_{\text{below}}(I) \simeq \frac{G^2 + D'(s_0)^2}{D'(s_0)\kappa_0 - A_J(I)G}. \quad (6)$$

Furthermore, by expressing the below-threshold gyration frequency as $f_{\text{below}}(I) = A_J(I)/(2\pi D'(s_0))$ and using the fact that $\kappa_0/(2\pi G)$ corresponds to the conventional VSTO oscillation frequency f_{conv} in the above-threshold regime, we can rearrange the result into the compact form

$$\tau_{\text{below}}(I) = \tau_0 \left(1 - \frac{f_{\text{below}}(I)}{f_{\text{conv}}} \right)^{-1}, \quad (7)$$

where $\tau_0 = \frac{G^2 + D'(s_0)^2}{D'(s_0)\kappa_0}$ is the transient time at zero current within this linearized model. This estimate is consistent with Fig. 4: it explains the emergence of $\lambda < 0$ near $I \simeq 0$ for $t_p \geq 7$ ns and the divergence of τ_{below} as $I \rightarrow I_{\text{th}}$, which confines the $\lambda > 0$ region to a narrow band near the threshold for larger t_p .

These results suggest that increasing the pulse width enlarges the below-threshold region where the Lyapunov exponent becomes negative, and that the parameter region exhibiting high learning-performance metrics expands accordingly. Figure 5 shows the dependence of the information processing capacity (IPC) on the external-field strength and the dc current for pulse widths $t_p = 7$ and 10 ns. As t_p increases, the IPC increases overall, and, in particular, the region with high IPC below the threshold current expands markedly. Therefore, by appropriately tuning the input pulse width, the m-VSTO can operate as a physical reservoir with high learning performance in the low-current and low-field regime.

In summary, we systematically evaluated the vortex-core dynamics and the learning performance of an m-VSTO as a physical reservoir by numerical simulations based on the Thiele equation. The AL on the free layer transforms the potential landscape into a Mexican-hat-like form, so that oscillations arise even in the below-threshold, low-current and low-field regime where a conventional VSTO exhibits little dynamics, and chaotic behavior is also observed. In this low-current and low-field regime, both STMC and IPC take finite values, and, in particular, around $h_0 \simeq 1$ Oe and $I \simeq 1$ mA, we found that the m-VSTO achieves an IPC approximately twice that of a conventional VSTO with about one quarter of the power consumption. We further demonstrated that choosing the input pulse width to be comparable to, or longer than, the transient time expands both the region where the Lyapunov exponent is negative below the threshold current and the region exhibiting high STMC/IPC. These results indicate that the coordinated design of the potential landscape and the driving conditions is key to improving the learning performance and reducing the power consumption of m-VSTO reservoirs. Overall, our study demonstrates the feasibility of energy-efficient physical reservoirs based on vortex spin-torque oscillators.

ACKNOWLEDGMENTS

This work was partly supported by Grants-in-Aid for Scientific Research (Grants No. 24K00916, 24H00018, 22K14591, 24K06912) from the Japan Society for the Promotion of

Science and Amano Institute of Technology. The authors would like to express our deepest gratitude to Dr. Tomohiro Taniguchi (AIST) for helpful advice and discussions on the STMC calculation method. This work was partially performed under the Research Program of “Dynamic Alliance for Open Innovation Bridging Human, Environment and Materials” in “Network Joint Research Center for Materials and Devices.”

REFERENCES

- ¹M. Lukosevicius and H. Jaeger, *Comput. Sci. Rev.* **3**, 127–149 (2009).
- ²G. Tanaka, T. Yamane, J. B. Héroux, R. Nakane, N. Kanazawa, S. Takeda, H. Numata, D. Nakano, and A. Hirose, *Neural Netw.* **115**, 100–123 (2019).
- ³C. G. Langton, *Physica D* **42**, 12–37 (1990).
- ⁴J. Boedecker, O. Obst, J. T. Lizier, N. M. Mayer, and M. Asada, *Theory Biosci.* **131**, 205–213 (2012).
- ⁵D. Wang, Y. Nie, G. Hu, H. K. Tsang, and C. Huang, *Nat. Commun.* **15**, 10841 (2024).
- ⁶J. Sun, W. Yang, T. Zheng, X. Xiong, Y. Liu, Z. Wang, Z. Li, and X. Zou, *Microsyst. Nanoeng.* **7**, 83 (2021).
- ⁷T. Kanao, H. Suto, K. Mizushima, H. Goto, T. Tanamoto, and T. Nagasawa, *Phys. Rev. Applied* **12**, 024052 (2019).
- ⁸N. Akashi, T. Yamaguchi, S. Tsunegi, T. Taniguchi, M. Nishida, R. Sakurai, Y. Wakao, and K. Nakajima, *Phys. Rev. Research* **2**, 043303 (2020).
- ⁹T. Yamaguchi, S. Tsunegi, K. Nakajima, and T. Taniguchi, *Phys. Rev. B* **107**, 054406 (2023).
- ¹⁰W. Namiki, D. Nishioka, T. Tsuchiya, and K. Terabe, *Neuromorph. Comput. Eng.* **4**, 024015 (2024).
- ¹¹R. Tatsumi, T. Chiba, T. Komine, and H. Matsueda, *Phys. Rev. E* **111**, 064202 (2025).
- ¹²S. Tsunegi, T. Taniguchi, K. Nakajima, S. Miwa, K. Yakushiji, A. Fukushima, S. Yuasa, and H. Kubota, *Appl. Phys. Lett.* **114**, 164101 (2019).
- ¹³A. R. Ismail, S. Jovanovic, S. Petit-Watelot, and H. Rabah, *Electronics* **8**, 1315 (2019).
- ¹⁴T. Yamaguchi, N. Akashi, K. Nakajima, H. Kubota, S. Tsunegi, and T. Taniguchi, *Sci. Rep.* **10**, 19536 (2020).
- ¹⁵T. Taniguchi, A. Ogihara, Y. Utsumi, and S. Tsunegi, *Sci. Rep.* **12**, 10627 (2022).

- ¹⁶S. Shreya, A. Jenkins, I. Rezaeiyan, G. Li, K. D. Bohnert, M. Benetti, R. Ferreira, H. Moradi, and H. Farkhani, *Sci. Rep.* **13**, 16722 (2023).
- ¹⁷H. Shen, L. Xu, M. Jin, H. Li, C. Yu, B. Liu, and T. Zhou, *Nanotechnology* **35**, 415201 (2024).
- ¹⁸V. S. Pribiag et al., *Nat. Phys.* **3**, 498–503 (2007).
- ¹⁹T. Yamamoto, T. Seki, and K. Takanashi, *Phys. Rev. B* **94**, 094419 (2016).
- ²⁰A. Kamimaki et al., *Phys. Rev. Research* **3**, 043216 (2021).
- ²¹M. Inubushi and K. Yoshimura, *Sci. Rep.* **7**, 10199 (2017).
- ²²J. Dambre et al., *Sci. Rep.* **2**, 514 (2012).
- ²³C. Teuscher, *Biosystems* **218**, 104693 (2022).
- ²⁴Y. Imai et al., *Sci. Rep.* **12**, 21651 (2022).
- ²⁵K. Horizumi, T. Chiba, and T. Komine, *J. Magn. Soc. Jpn.* **49**, 42–46 (2025).
- ²⁶K. Horizumi, T. Chiba, and T. Komine, *IEEE Trans. Magn.* **61**, 1400405 (2025).
- ²⁷S. Petit-Watelot et al., *Nat. Phys.* **8**, 682–687 (2012).
- ²⁸T. Devolder et al., *Phys. Rev. Lett.* **123**, 147701 (2019).
- ²⁹S. H. Strogatz, *Nonlinear Dynamics and Chaos* (Westview, 2001).
- ³⁰A. A. Thiele, *Phys. Rev. Lett.* **30**, 230–233 (1973).
- ³¹A. Dussaux et al., *Phys. Rev. B* **86**, 014402 (2012).
- ³²E. Grimaldi et al., *Phys. Rev. B* **89**, 104404 (2014).
- ³³S. Tsunegi et al., *Sci. Rep.* **11**, 16285 (2021).
- ³⁴A. Vansteenkiste et al., *AIP Adv.* **4**, 107133 (2014).
- ³⁵K. Y. Guslienko et al., *Nanoscale Res. Lett.* **9**, 386 (2014).
- ³⁶I. Shimada and T. Nagashima, *Prog. Theor. Phys.* **61**, 1605 (1979).
- ³⁷M. Lukosevicius and H. Jaeger, *Comput. Sci. Rev.* **3**, 127–149 (2009).
- ³⁸G. Tanaka, T. Yamane, J. B. Héroux, R. Nakane, N. Kanazawa, S. Takeda, H. Numata, D. Nakano, and A. Hirose, *Neural Netw.* **115**, 100–123 (2019).
- ³⁹C. G. Langton, *Physica D* **42**, 12–37 (1990).
- ⁴⁰J. Boedecker, O. Obst, J. T. Lizier, N. M. Mayer, and M. Asada, *Theory Biosci.* **131**, 205–213 (2012).
- ⁴¹D. Wang, Y. Nie, G. Hu, H. K. Tsang, and C. Huang, *Nat. Commun.* **15**, 10841 (2024).
- ⁴²J. Sun, W. Yang, T. Zheng, X. Xiong, Y. Liu, Z. Wang, Z. Li, and X. Zou, *Microsyst. Nanoeng.* **7**, 83 (2021).

- ⁴³T. Kanao, H. Suto, K. Mizushima, H. Goto, T. Tanamoto, and T. Nagasawa, *Phys. Rev. Applied* **12**, 024052 (2019).
- ⁴⁴N. Akashi, T. Yamaguchi, S. Tsunegi, T. Taniguchi, M. Nishida, R. Sakurai, Y. Wakao, and K. Nakajima, *Phys. Rev. Research* **2**, 043303 (2020).
- ⁴⁵T. Yamaguchi, S. Tsunegi, K. Nakajima, and T. Taniguchi, *Phys. Rev. B* **107**, 054406 (2023).
- ⁴⁶W. Namiki, D. Nishioka, T. Tsuchiya, and K. Terabe, *Neuromorph. Comput. Eng.* **4**, 024015 (2024).
- ⁴⁷R. Tatsumi, T. Chiba, T. Komine, and H. Matsueda, *Phys. Rev. E* **111**, 064202 (2025).
- ⁴⁸S. Tsunegi, T. Taniguchi, K. Nakajima, S. Miwa, K. Yakushiji, A. Fukushima, S. Yuasa, and H. Kubota, *Appl. Phys. Lett.* **114**, 164101 (2019).
- ⁴⁹A. R. Ismail, S. Jovanovic, S. Petit-Watelot, and H. Rabah, *Electronics* **8**, 1315 (2019).
- ⁵⁰T. Yamaguchi, N. Akashi, K. Nakajima, H. Kubota, S. Tsunegi, and T. Taniguchi, *Sci. Rep.* **10**, 19536 (2020).
- ⁵¹T. Taniguchi, A. Ogihara, Y. Utsumi, and S. Tsunegi, *Sci. Rep.* **12**, 10627 (2022).
- ⁵²S. Shreya, A. Jenkins, I. Rezaeiyan, G. Li, K. D. Bohnert, M. Benetti, R. Ferreira, H. Moradi, and H. Farkhani, *Sci. Rep.* **13**, 16722 (2023).
- ⁵³H. Shen, L. Xu, M. Jin, H. Li, C. Yu, B. Liu, and T. Zhou, *Nanotechnology* **35**, 415201 (2024).
- ⁵⁴V. S. Pribiag et al., *Nat. Phys.* **3**, 498–503 (2007).
- ⁵⁵T. Yamamoto, T. Seki, and K. Takanashi, *Phys. Rev. B* **94**, 094419 (2016).
- ⁵⁶A. Kamimaki et al., *Phys. Rev. Research* **3**, 043216 (2021).
- ⁵⁷M. Inubushi and K. Yoshimura, *Sci. Rep.* **7**, 10199 (2017).
- ⁵⁸J. Dambre et al., *Sci. Rep.* **2**, 514 (2012).
- ⁵⁹C. Teuscher, *Biosystems* **218**, 104693 (2022).
- ⁶⁰Y. Imai et al., *Sci. Rep.* **12**, 21651 (2022).
- ⁶¹K. Horizumi, T. Chiba, and T. Komine, *J. Magn. Soc. Jpn.* **49**, 42–46 (2025).
- ⁶²K. Horizumi, T. Chiba, and T. Komine, *IEEE Trans. Magn.* **61**, 1400405 (2025).
- ⁶³S. Petit-Watelot et al., *Nat. Phys.* **8**, 682–687 (2012).
- ⁶⁴T. Devolder et al., *Phys. Rev. Lett.* **123**, 147701 (2019).
- ⁶⁵S. H. Strogatz, *Nonlinear Dynamics and Chaos* (Westview, 2001).
- ⁶⁶A. A. Thiele, *Phys. Rev. Lett.* **30**, 230–233 (1973).

⁶⁷A. Dussaux et al., Phys. Rev. B **86**, 014402 (2012).

⁶⁸E. Grimaldi et al., Phys. Rev. B **89**, 104404 (2014).

⁶⁹S. Tsunegi et al., Sci. Rep. **11**, 16285 (2021).

⁷⁰A. Vansteenkiste et al., AIP Adv. **4**, 107133 (2014).

⁷¹K. Y. Guslienko et al., Nanoscale Res. Lett. **9**, 386 (2014).

⁷²I. Shimada and T. Nagashima, Prog. Theor. Phys. **61**, 1605 (1979).

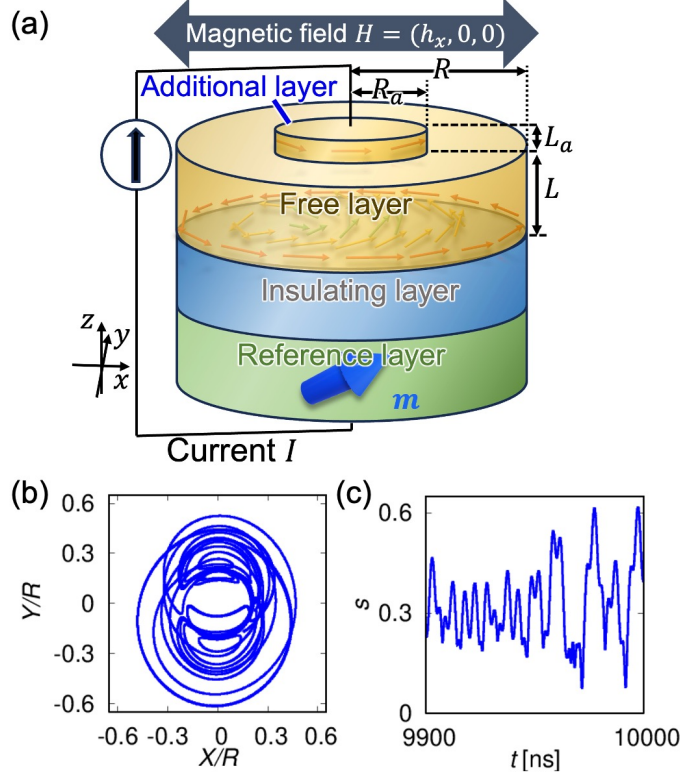


FIG. 1. (a) Schematic of the modified vortex spin-torque oscillator (m-VSTO). A circular ferromagnetic additional layer (AL) of radius R_a and thickness L_a is concentrically stacked on the free layer (radius R , thickness L) of a ferromagnet/insulator/ferromagnet trilayer. A dc current I is injected perpendicular to the film plane, and an in-plane magnetic field $\mathbf{H} = (h_x, 0, 0)$ is applied along the x axis; \mathbf{m} denotes the magnetization direction of the reference layer. (b),(c) Representative vortex-core dynamics under an x -directed sinusoidal ac magnetic field at $I = 0$: (b) phase portrait of the normalized vortex-core position $(X/R, Y/R)$ after discarding an initial transient and (c) the corresponding time trace of the normalized gyration amplitude $s(t)$. The aperiodic trajectory and irregular amplitude fluctuations indicate a chaotic response enabled by the AL-induced deformation of the confinement potential.

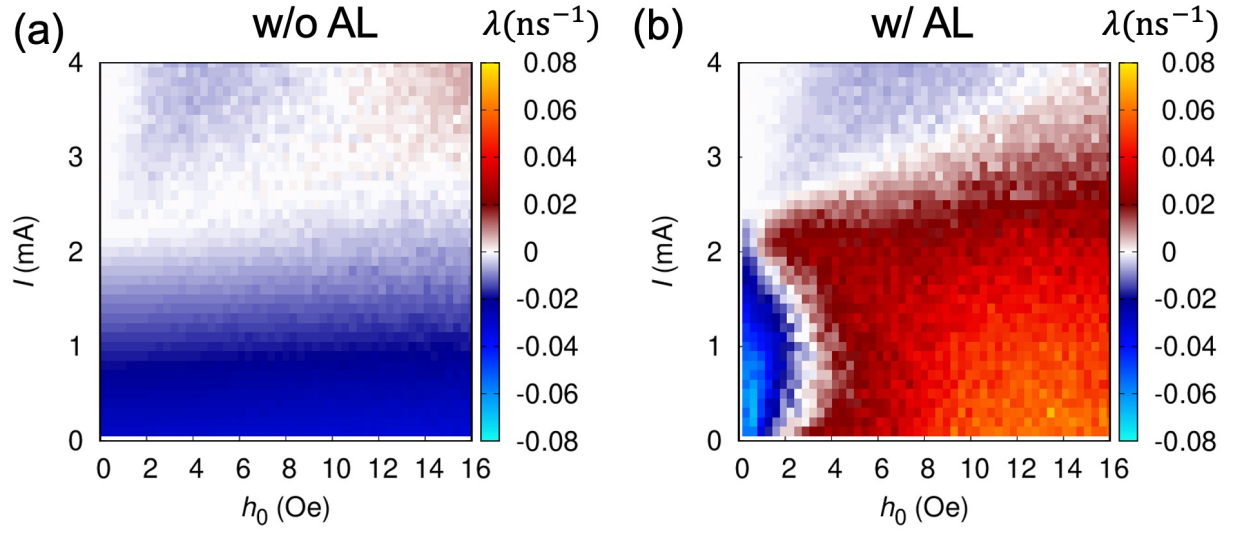


FIG. 2. Dependence of Lyapunov exponent λ on input strength h_0 (Oe) and current I (mA) for (a) without AL and (b) with AL radius $R_a = 40$ nm. White indicates a region where λ is very close to zero, which we regard as corresponding to the edge of chaos.

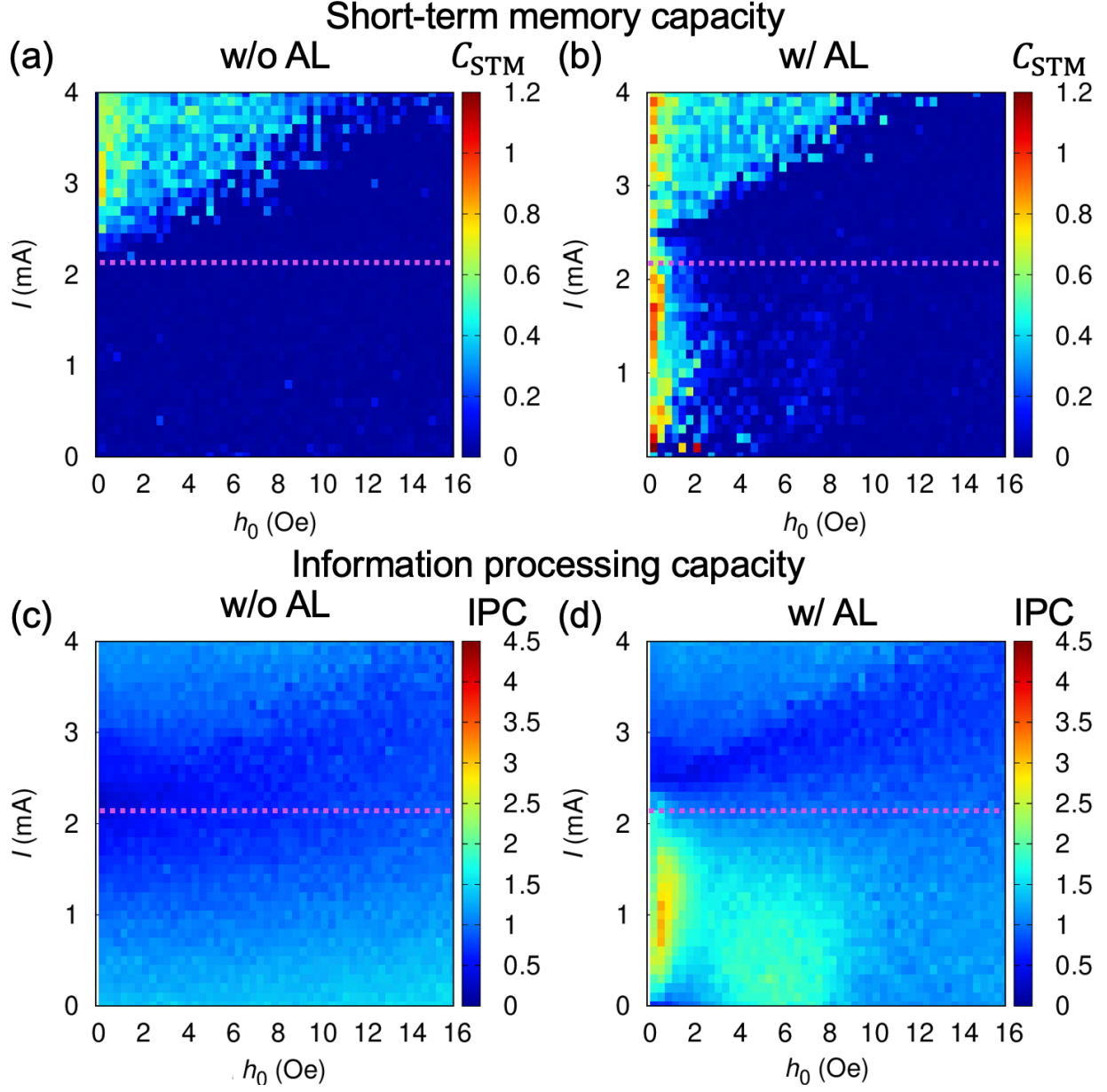


FIG. 3. Dependence of short-term memory capacity C_{STM} and information processing capacity (IPC) on input strength h_0 (Oe) and current I (mA) for (a)(c) without AL and (b)(d) with AL radius $R_a = 40$ nm. The purple dashed line indicates the threshold current of a conventional VSTO.

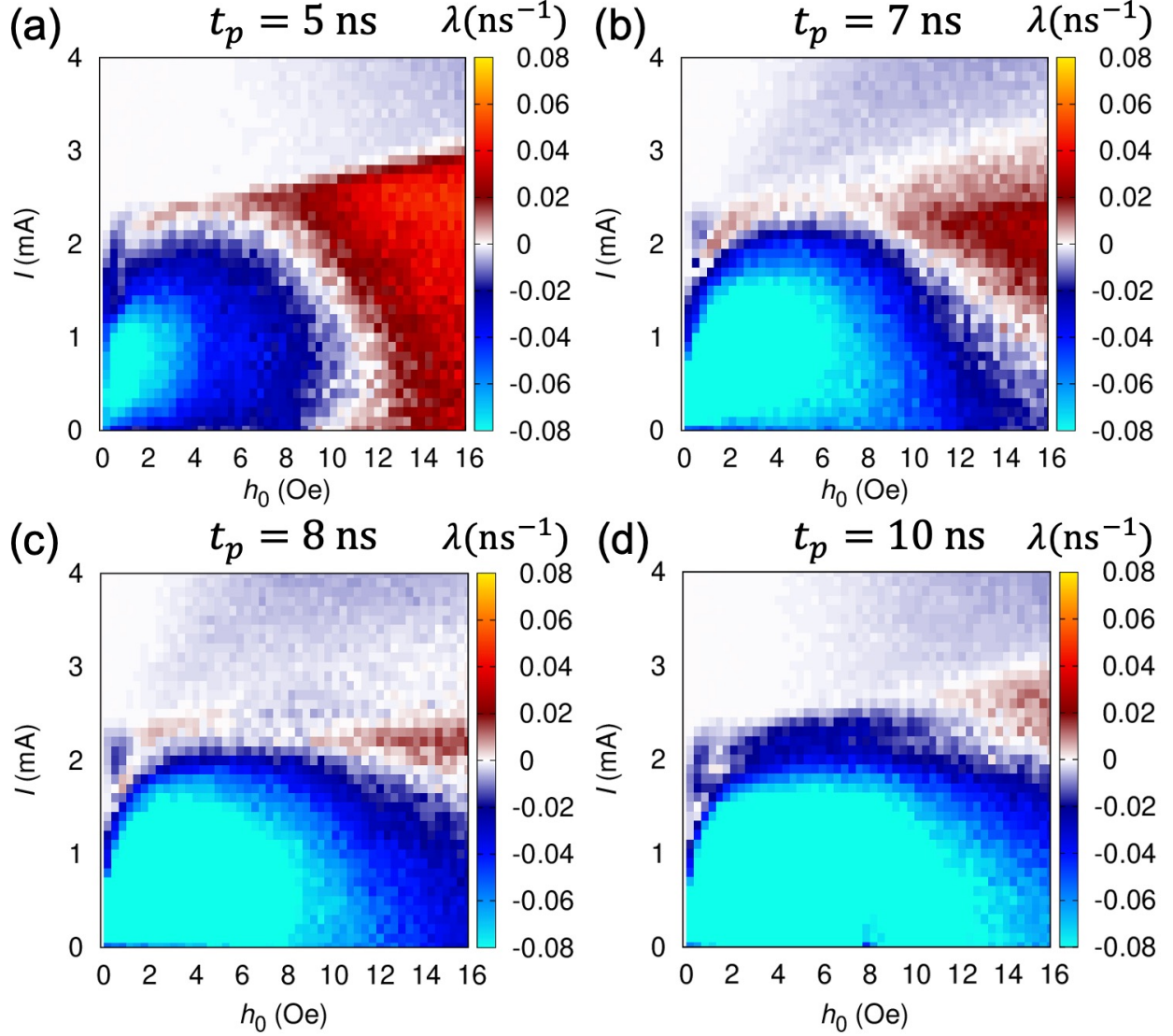


FIG. 4. Dependence of Lyapunov exponent λ on input strength h_0 (Oe) and current I (mA) for $R_a = 40$ nm with pulse widths (a) $t_p = 5$ ns, (b) $t_p = 7$ ns, (c) $t_p = 8$ ns, and (d) $t_p = 10$ ns. White indicates a region where λ is very close to zero, which we regard as corresponding to the edge of chaos.

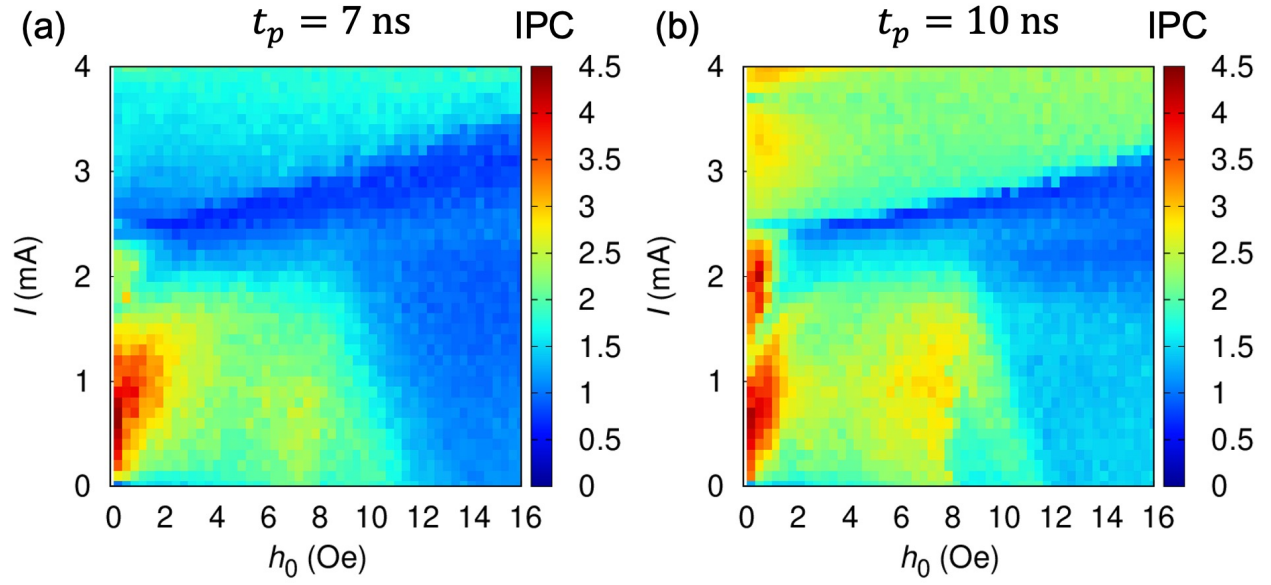


FIG. 5. Dependence of information processing capacity on input strength h_0 (Oe) and current I (mA) for $R_a = 40$ nm with pulse widths (a) $t_p = 7$ ns and (b) $t_p = 10$ ns.